# A Case Study of the Origin of Hail in a Multicell Thunderstorm Using In Situ Aircraft and Polarimetric Radar Data

PATRICK C. KENNEDY

*Department of Atmospheric Science, Colorado State University, Fort Collins, Colorado*

ANDREW G. DETWILER

*Department of Atmospheric Science, South Dakota School of Mines and Technology, Rapid City, South Dakota*

(Manuscript received 28 September 2002, in final form 12 May 2003)

ABSTRACT

An armored T-28 research aircraft made direct observations of the hydrometeors present at approximately the −3°C temperature level in the inflow region of a multicell thunderstorm. During the penetration, both the Colorado State University (CSU)–University of Chicago and Illinois State Water Survey (CHILL) 11-cm-wavelength dual-polarization research radar and the Denver, Colorado, Front Range Airport (KFTG) Weather Surveillance Radar-1988 Doppler (WSR-88D) were scanning this storm. Polarimetric radar indications of hail (high reflectivity and low differential reflectivity) appeared near the surface in the echo core adjacent to the aircraft track approximately 6 min after the T-28's inflow transit. Radial velocity data from the KFTG radar were combined with those recorded at CSU–CHILL to synthesize the airflow fields in the storm around the time of the T-28 penetration. Hail trajectories were initiated from a location at which the T-28 encountered a burst of approximately 1-cm-diameter, low-density graupel particles within the general storm inflow region. Forward-time trajectory calculations indicated that these graupel particles subsequently grew slightly into small hailstones and ended up within a few kilometers of the near-surface polarimetric radar hail-signature location. Trajectories computed backward in time imply that these hail embryos originated aloft in the forward portion of the echo complex. These are the first quantitative, direct in situ observations of recirculating precipitation becoming embryos for hail development.

## 1. Introduction

One tool used to study the development of precipitation and hail in thunderstorms is the computational particle trajectory model. Input to this model may be a three-dimensional wind field synthesized from multiple-Doppler radar data obtained from a thunderstorm case study or perhaps a wind field generated by a time-dependent three-dimensional cloud model simulating a thunderstorm. The trajectory model then uses these wind fields to advect growing particles, based upon assumptions about the distribution of cloud water, temperature, and other environmental characteristics important in the development of hail. Particles may originate as small embryos that grow in size as time progresses; the model follows their trajectories until these particles fall out of the cloud. The model can also reverse the process, identifying hydrometeors at locations at which hail was observed or expected and then calculating the earlier history of these particles as time moves backward. The resulting back trajectories are useful in identifying hail-embryo source regions.

Several trajectory studies of hail growth in a spectrum of High Plains convective storm types have been done based on multiple-Doppler radar-derived wind fields and associated radar, aircraft, and surface observations from the National Hail Research Experiment (NHRE) and the Cooperative Convective Precipitation Experiment (CCOPE). The NHRE project was conducted from 1972 to 1976 in northeastern Colorado and southeastern Wyoming, and CCOPE was conducted in 1981 in southeastern Montana. The spectrum of storms studied spanned a range of sizes and structures from multicellular- to supercellular-type storms. Heymsfield et al. (1980), Dye et al. (1983), Miller et al. (1983), and Heymsfield (1983), for instance, did trajectory studies using radar-derived wind fields from small- to moderate-sized multicellular hail storms observed during NHRE. Knight and Knupp (1986) studied a similar storm from CCOPE. These studies showed that hail could develop along many different trajectories within these types of storms. In general, it was deduced that hail did not often develop to significant (diameter $> \sim 1$ cm) size unless

*Corresponding author address:* Mr. Patrick C. Kennedy, Department of Atmospheric Science, Colorado State University, Fort Collins, CO 80523-1381.
E-mail: pat@lab.chill.colostate.edu

it grew from embryos that first developed to millimeter sizes in flanking or feeder cells with relatively modest updrafts. These embryos were then transported in some way into storm-core regions with stronger updrafts and higher supercooled liquid water concentrations, in which regions they could be suspended as they grew into hail. One class of plausible trajectories involved large aggregates in the upshear overhang region of a cell, or in the upper regions of neighboring cells, being transported into a primary updraft region in the same or a neighboring cell. Transport from flanking cells into core (primary) updraft regions might also occur at midlevels within the storm, with the embryos entering the primary cell at these heights and growing there until they either exited the updraft or became massive enough to fall through it. Other trajectories resulting in hail originated with embryos that precipitated out of flanking cells, or the upshear overhang of the same cell, and were ingested into the core updraft at low levels (possibly falling below the melting level before being ingested). These particles subsequently rose and grew by accretion of supercooled water in the core updraft and then became large enough to descend out of the storm. Growth from cloud droplets, drizzle, and small ice particle sizes to hail sizes entirely within a core updraft, starting with cloud droplets at cloud base, typically is not possible because such growing particles are lofted into the anvil region by strong updrafts before they can grow into hail.

Miller et al. (1988, 1990) did similar studies using data from larger, more steady-state storms observed during CCOPE. As in the NHRE storms, it was observed that many different plausible growth trajectories could lead to the development of hail. In almost all cases, the growth trajectories from embryo to hail sizes were simple up-and-down, nearly straight-line paths. Complicated looping trajectories were uncommon, although it should be noted that the airflow fields synthesized from multiple-Doppler measurements are significantly smoothed in time and space. The actual trajectories may well be more complex. In many cases, the obstaclelike flow that develops as the environmental winds diverge around updraft cores and carry surface-layer momentum upward was instrumental in carrying embryos from flanking cells on the upshear side around to the sides of updrafts in the main part of the storm. Thus, these upshear cells have been recognized as likely sources for hail embryos.

These trajectory studies were based on Doppler radar data. Dual-wavelength radar data (occasionally supported by surface observations) were also used to infer the presence of hail, but hail embryo types and concentrations could not be unambiguously identified using radar. In some cases, aircraft microphysical data were available in general regions that were inferred at one time or another to be source regions for hail embryos, and the characteristics of these embryos could be observed (Dye et al. 1983). In other cases aircraft data confirmed the presence of graupel and hail at midlevels in the storms in locations similar to those identified along plausible growth trajectories (e.g., Heymsfield et al. 1980; Dye et al. 1983; Miller et al. 1990). The in situ data generally supported the inferences based on the trajectory calculations and were invaluable in discriminating between embryo types. However, none of these prior studies directly documented the presence of recirculating hail embryos at cloud-base heights.

We report here observations of a multicellular High Plains hailstorm that occurred in the same region as storms observed during NHRE. Doppler radar–derived wind fields are used to calculate the trajectories along which radar-identified hail developed during one phase of the storm's life. In situ aircraft observations identified localized concentrations of low-density graupel particles entering the core updraft in a region for which trajectory analysis indicated that the radar-identified hail was growing. The results imply that these graupel particles then grew into small hailstones along a simple up-and-down trajectory and reached the surface ~6 min later. These detailed, time-resolved observations reinforce the conclusions based on previous studies that hail production in multicellular storms is often episodic and is dependent on fortuitous arrangements of neighboring updraft cores and associated flanking cells and mid- and upper-level anvil regions.

The paper begins with an overview of the storm and the primary observational datasets. The radar data analyses are then used to provide a framework in which the detailed T-28 observations are placed. The paper concludes with a discussion of the hail trajectory implications in the context of prior studies of mutlicellular hailstorms.

## 2. Storm overview

The primary observing systems employed in this study were the Colorado State University (CSU)–University of Chicago and Illinois State Water Survey (CHILL) multiparameter research radar (Brunkow et al. 2000), the Denver, Colorado, Front Range Airport (KFTG) National Weather Service (NWS) Weather Surveillance Radar-1988 Doppler (WSR-88D), and the South Dakota School of Mines and Technology (SDSMT) armored T-28 storm-penetration aircraft (Johnson and Smith 1980). (At the time of writing, comprehensive technical data for the T-28 were available online at http://www.ias.sdsmt.edu/institute/t28/index.htm and data for the CSU–CHILL were available online at http://www.chill.colostate.edu/.) Microphysical characteristics within various regions of the storm were diagnosed using the dual-polarimetric parameters obtained from CSU–CHILL, and cloud water and precipitation particle image data were obtained by the T-28. This T-28 flight was conducted during an aircraft instrumentation test program; it was not specifically planned to support a detailed storm microphysical study.

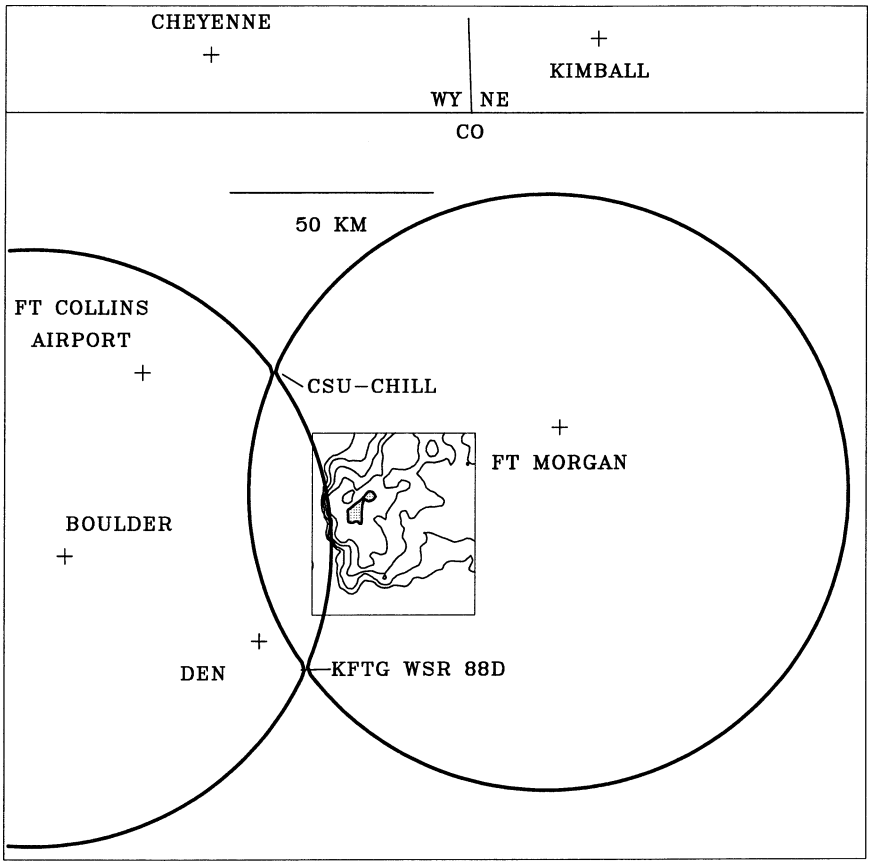


FIG. 1. The eastern lobe of the CSU–CHILL KFTG WSR-88D dual-Doppler coverage area. Beam intersection angles are at least 30° within the depicted lobe. The inset plot shows the CSU–CHILL reflectivity contours (starting value of 10 dBZ, step of 10 dB, and levels above 50 dBZ shaded) at the 4.8-km-MSL height level at 2254 UTC 22 Jun 1998.

However, the unique observations obtained during the test flight led us to develop the analysis presented below.

During the afternoon of 22 June 1998, the storm that was targeted for aircraft penetrations originally developed along a preexisting outflow boundary approximately 20 km northwest of the Denver International Airport (DEN). The storm then moved east-northeastward at about 8 m $s^{-1}$. Low-level outflow from it produced a distinct fine-line echo that advanced ahead of the precipitation echo around the southeastern end of the storm. The enhanced convergence along this outflow boundary was probably responsible for the new reflectivity cores that periodically were observed to form within the southernmost portion of the echo system. The aircraft was launched at 2145 UTC (all times in this paper are in UTC; local daylight time = UTC − 6 h) and began a series of passes across the general inflow region of the multicellular echo complex at an altitude of 4.8 km MSL (just above the freezing–melting level). By 2254 UTC, the storm was centered approximately 30 km northeast of DEN (Fig. 1). At the height shown in Fig. 1 (4.8 km MSL), reflectivities in excess of 50 dBZ existed only within the central region of the echo; an axis of relatively high reflectivities projected southward from the 50-dBZ core.

The three-dimensional flow fields in the storm were obtained from dual-Doppler analyses performed at times shortly before and after the final T-28 pass (2255:36–2300:05). The relevant KFTG WSR-88D volume scan data were extracted from a level-II archive tape (Crum et al. 1993) and converted to universal Doppler exchange format (UF; Barnes 1980). The UF data from both the WSR-88D and the CSU–CHILL radars were interactively edited to remove contamination from noise, antenna beam pattern sidelobe artifacts, and ground clutter. Radial velocities were interactively dealiased.

The resultant edited polar-coordinate data were interpolated to a three-dimensional Cartesian gridpoint mesh (1-km spacing in both the horizontal and vertical directions) using a Cressman weighting (Cressman 1959). The WSR-88D was operating in volume-coverage-precipitation mode 11 (Wood and Brown 1997), and so the elevation-angle step sizes were fairly coarse. This was partially compensated for by the modest range (~40–50 km) from KFTG to the echo region of greatest

interest.) Because of the differences in the elevation-angle step sizes, the WSR-88D data interpolation used a limiting vertical-plane radius of 1.5 km; the corresponding radius limit in the CSU–CHILL interpolations was 0.75 km. In the horizontal plane, the interpolation radius of influence was 1.0 km for both radars. The spatial resolution of the resultant dual-Doppler flow fields is coarse, with poor resolution of features smaller than 4–6 km. The gridded radial velocities were the only WSR-88D data field used in the analyses.

Horizontal wind field syntheses based on the gridded radial velocities were done via the Custom Editing and Display of Reduced Information in Cartesian Space (CEDRIC) software package (Mohr et al. 1986). A correction for echo advection based on the radar-observed storm motion was applied during the syntheses, producing three primary analyses valid at 2247, 2252, and 2306. (During the intermediate times the elevation angles scanned by the CSU–CHILL radar were restricted to the T-28's immediate area. Thus, dual-Doppler wind field recoveries were not possible because of the incomplete volumetric scan coverage.) In each analysis, the three synthesized airflow components were iteratively adjusted to account for the effects of vertical motions on the horizontal winds obtained from the dual-Doppler equations. Divergence fields were calculated from the adjusted horizontal winds at each analysis height. Vertical airflow was obtained by vertically integrating these horizontal divergence fields. The integration procedure imposed a variational constraint that forced the vertical velocities to 0 m $s^{-1}$ at the endpoints of the integration paths.

The 2252 dual-Doppler constant-altitude plan position indicator (CAPPI) analysis at the 4.8-km-MSL height level (the nominal T-28 flight altitude) is shown in Fig. 2a. At this time, the T-28 was starting a southwestbound pass. The reflectivity contours curve in toward the echo core in the region where the strongest storm-relative inflow ($X = 28$, $Y = -38$ km) was located. The maximum updraft analyzed along the flight path at this height was also located in the general inflow area ($X = 29$, $Y = -41$ km). A mesoanticyclonic circulation was centered near $X = 24$, $Y = -32$ km.

The low-level (2.8 km MSL, approximately 1.4 km AGL) storm-relative flow field at 2252 is shown in Fig. 2b. The strongest updrafts continued to be found in close proximity to the slight kink in the T-28 flight track ($X = 30$, $Y = -40$ km). Storm-relative inflow was maximum in this same area.

The 2306 analysis, 6 min after the time of primary interest during the T-28 pass, is shown in Fig. 3a. Many of the larger-scale horizontal flow features, including the broad southeasterly inflow and the mesoanticyclone, are still evident. An appreciable reflectivity increase had taken place in the southern end of the echo system between 2252 and 2306 ($X = 31$, $Y = -43$ km). The area enclosed by the 15 m $s^{-1}$ updraft contours had also similarly expanded ($X = 35$, $Y = -40$ km). Farther to

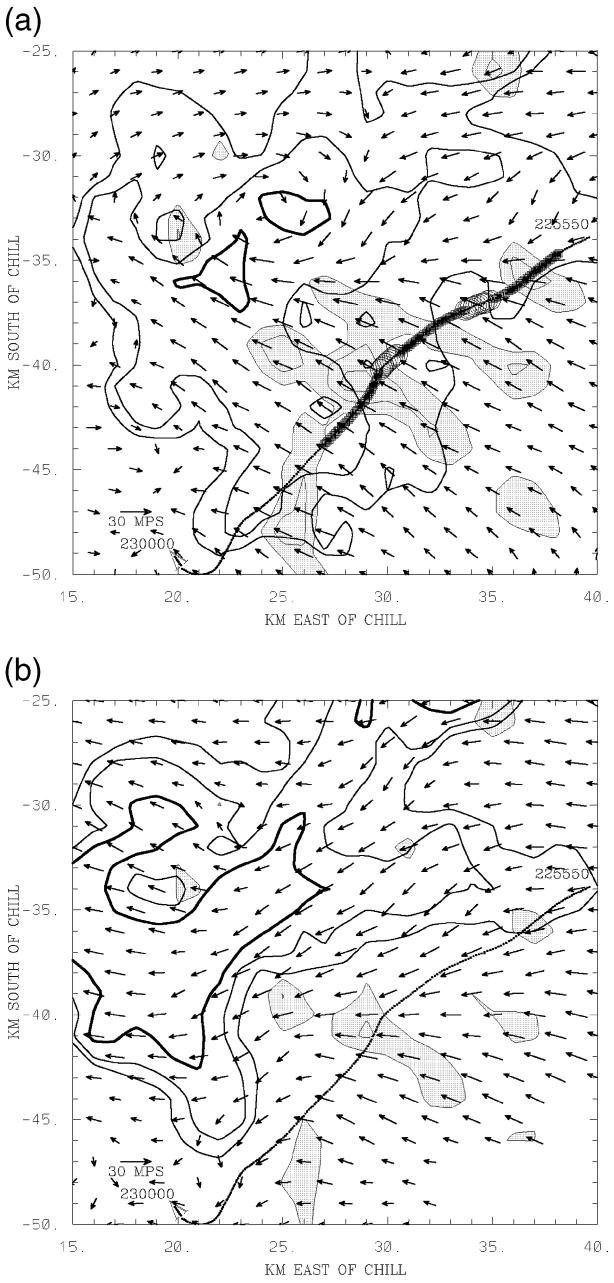


FIG. 2. (a) Dual-Doppler analysis at 2252 UTC 22 Jun 1998. Height level is 4.8 km MSL; thick contours are CSU–CHILL reflectivity levels (starting value is 30 dB*Z*, interval is 10 dB, and heavy contour is 50 dBZ). Horizontal wind vectors are storm relative; scaling vector is shown near the lower left-hand corner of the plot. Updrafts $> 10$ m $s^{-1}$ are stippled; updraft contour interval is 5 m $s^{-1}$. Symbols on the T-28 track indicate the aircraft-sensed vertical air motions. Squares are updrafts and open circles are downdrafts (see Fig. 5 for details). (b) Same as in (a) except CAPPI height level is 2.8 km MSL. Because this height is 2 km below the T-28's altitude, the updraft and downdraft symbols along the aircraft track have been removed.

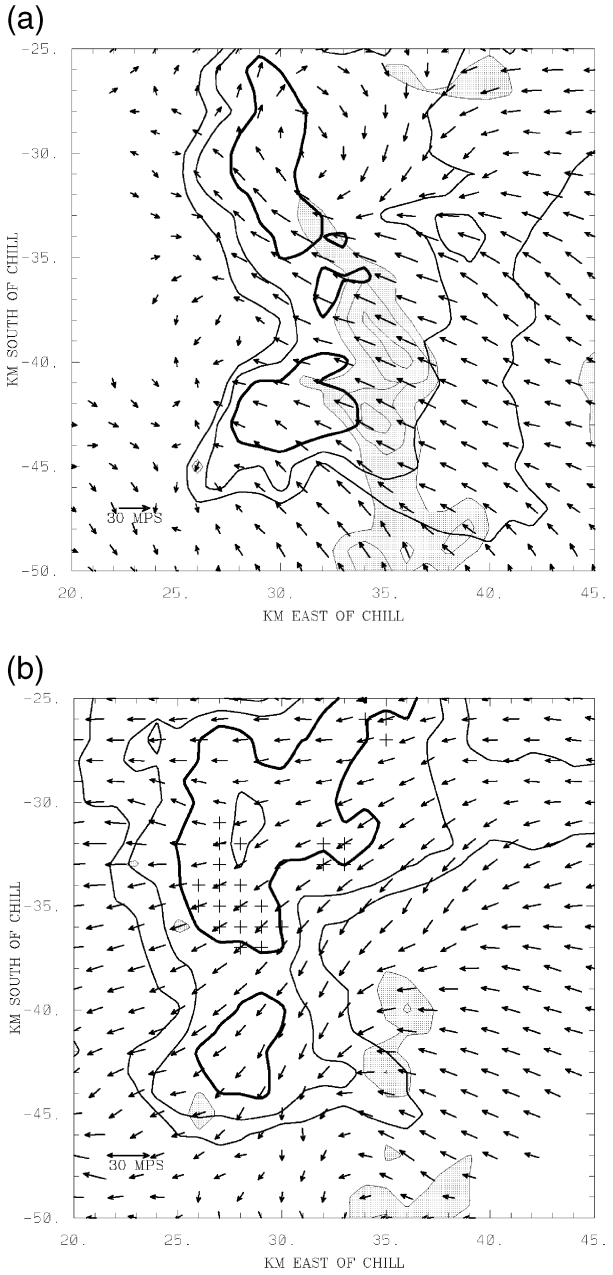


FIG. 3. (a) Same as in Fig. 2a, except the analysis time is 2306 UTC. (b) Dual-Doppler analysis at 2306 UTC at the 1.8-km-MSL height level. Horizontal wind vectors and reflectivity contours are as in Fig. 2b. Cross symbols depict grid points at which the HDR values exceed 0 dB (i.e., the presence of hail is indicated; see text for details).

the north ($X = 31$, $Y = -31$ km), an elongated 50-dB$Z$ echo core had evolved from the two separate, smaller cores that had been present at 2252.

The 2306 1.8-km-MSL CAPPI plot is shown in Fig. 3b. The cross symbols mark the grid points at which the hail differential reflectivity (HDR; Aydin et al. 1986) values exceed 0 dB. As formulated by Aydin et al., HDR is calculated by subtracting a prescribed function of differential reflectivity ($Z_{dr}$) from the reflectivity obtained when horizontal polarization is used for both transmission and reception ($Z_H$):

$$\text{HDR(db)} = Z_H - f(Z_{dr}), \tag{1}$$

where

$$f(Z_{dr}) = \begin{cases} 27 & \text{when } Z_{dr} \le 0 \text{ dB} \\ 19Z_{dr} + 27 & \text{when } 0 \le Z_{dr} \le 1.74 \text{ dB} \\ 60 & \text{when } Z_{dr} > 1.74 \text{ dB}; \quad \text{and} \end{cases}$$

$$Z_{dr}\ (\text{dB}) = 10 \log_{10}(Z_{HH}/Z_{VV}); \tag{2}$$

where $Z_{HH}$ is the copolar reflectivity at horizontal polarization and $Z_{VV}$ is the copolar reflectivity at vertical polarization.

HDR is a diagnostic parameter that becomes increasingly positive when the $Z_{dr}$ values decrease toward 0 dB in high-$Z_H$ regions. The canting-angle deviations of freely falling ice particles (several tens of degrees; Jayaweera and Mason 1965) greatly exceed the canting-angle variations of raindrops ($<10°$). Because of these appreciable orientation fluctuations, the $Z_{HH}$ and $Z_{VV}$ returns from large ice particles, such as graupel and hail, approach equality, lowering the $Z_{dr}$ value toward 0 dB. In contrast, because of aerodynamic forces, falling raindrops larger than approximately 1 mm in diameter assume an oblate horizontal cross-sectional shape (Pruppacher and Beard 1970). The raindrop's preferred shape and orientation properties tend to make $Z_{dr}$ positive ($Z_{HH} > Z_{VV}$). Thus, the cohesive cluster of grid points with HDR values in excess of 0 dB ($X = 27$, $Y = -35$ km in Fig. 3b) indicates that hail was becoming an increasingly large component of the near-surface precipitation that was being produced by the northern reflectivity core at this time. This HDR hail signature was fairly short lived and no longer existed after ~2320. The area containing this HDR hail signature is sparsely populated, and so no information was available from ground observers pertaining to the hail's existence, size, areal coverage, and so on. Note that the HDR hail signature associated with the developing cell at the southern end of the echo system eventually became fairly large and well defined. This southern HDR hail signature did correlate with a severe-weather spotter report of 19-mm-diameter hail that was received at the Denver NWS office at 2322 UTC.

The dual-Doppler analysis at 8.8 km MSL at 2306 is shown in Fig. 4; this height level is approximately 4 km above the T-28 pass altitude. It is apparent that the strongest updrafts (peak values $> 30$ m s$^{-1}$) were found in the southern portion of the echo system at this time. The horizontally diverging outflow associated with this updraft caused a southwesterly storm-relative flow to exist above the lower-altitude inflow region ($X = 37$, $Y = -40$ km). No reflectivities of more than 50 dB$Z$ were found at the 8.8-km height level above the HDR-indicated surface hail region. Examination of intervening-level CAPPIs suggested a tenuous connection at best

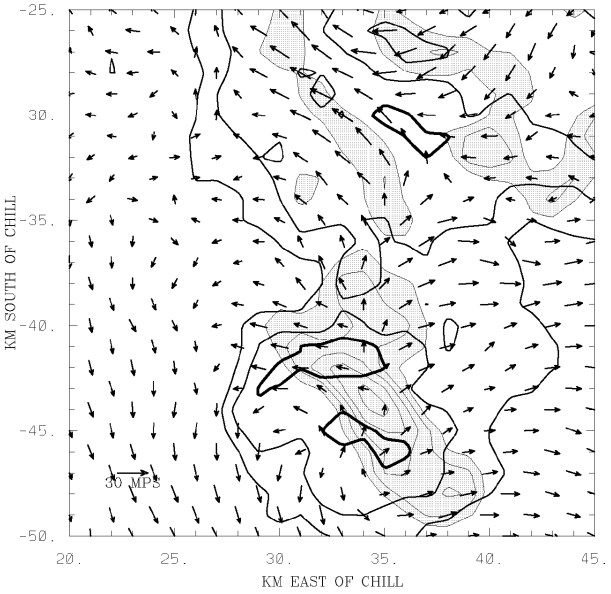


FIG. 4. Same as in Fig. 3a, except the analysis height is 8.8 km MSL.

between the small echo core centered at $X = 37$, $Y = -31$ km at the 8.8-km level and the elongated 50-dB$Z$ echo core noted at 4.8 km (Fig. 3).

Taken together, the analyses presented above reveal the evolving nature of the multicellular storm that the T-28 was penetrating. Throughout the analyzed time period, a broad southeasterly storm-relative inflow prevailed in the eastern portion of the echo system near the T-28 flight altitude. By 2306, the strongest updrafts had shifted to the southern end of the echo system in association with a semi-independently developing new cell. As this new cell was intensifying, hail began to reach the surface approximately 10 km farther north, beneath an older echo core.

## 3. T-28 in situ observations

An important hydrometeor sensor in the T-28's instrumentation suite is a high-volume precipitation spectrometer (HVPS) probe, which is commercially built by Stratton Park Engineering Corporation (SPEC), Inc. This instrument uses laser-beam illumination to develop shadow images of precipitation particles as they pass a 4.5-cm-wide, 256-element photodiode array. At a true airspeed of 100 m $s^{-1}$, the HVPS has a volumetric sampling rate of 1 $m^3$ $s^{-1}$, approximately 6 times that achieved by the older Particle Measuring Systems (PMS), Inc., OAP-2D-P optical sampling probes, but with similar 200-$\mu$m resolution. This increased sampling volume improves the probability of observing the larger-diameter, less numerous particles that make a significant contribution to the radar-backscattering characteristics of the precipitation. In addition to the HVPS probe, the T-28 also carried a coarser-imaging optical hail spectrometer developed at SDSMT to categorize the diameters of particles in the 0.5–4.5-cm size range with 0.9-mm resolution. The T-28 was equipped with a PMS forward scattering spectrometer probe and Droplet Measurement Technologies (DMT), Inc., liquid water sensor for sampling cloud water and with additional sensors for the normal atmospheric state variables. A microphone attached to the forward windscreen was recorded onto one of two audio channels of the flight video recorder. Impacts of solid hail on the windscreen can be heard on this channel.

The T-28 pass of interest here took place between approximately 2253 and 2300. The average altitude during this pass was 4.8 km MSL. As the pass progressed southwestward, the average observed air temperature gradually warmed from an initial value of about $-4$°C to about $-2$°C; at no time did it exceed 0°C. Local temperature fluctuations of about $\pm 2$°C took place in updrafts and downdrafts, respectively. Based on GPS position information that was being telemetered to the CSU–CHILL operations van and displayed in real time, the T-28 was vectored to fly near the band of maximum radial velocity convergence within the eastern (leading) portion of the echo. The resultant track is included in Fig. 2. As the T-28 crossed the general storm inflow area, the track deviated to the northwest as the strongest inflow was traversed.

Selected T-28 observations from the pass have been combined in Fig. 5. Of particular interest in these data are the alternating series of updrafts and downdrafts (i.e., U1, D1, U2, etc.) that were encountered between 2256 and 2258 within the general inflow notch in the reflectivity pattern. To correlate the radar and aircraft data, the aircraft track in Fig. 2 has been coded according to the times identified with U1, D1, and so on, in Fig. 5. The times associated with the T-28 track points plotted in Fig. 2 were approximately 5 min later than the radar analysis shown in the figure. Nevertheless, fairly good correlation is still apparent between the updrafts observed by the T-28 and the larger-scale features deduced from the dual-Doppler synthesis. The detailed T-28 observations suggest that the microphysical composition of the three aircraft-detected updrafts varied as the aircraft proceeded southwestward. The concentration of precipitation-sized particles (diameter $> 200$ $\mu$m) tended to increase in each of the successively encountered updrafts. In contrast, the cloud water concentrations tended to decrease in the successive updraft encounters.

Samples from HVPS image records collected at various points along the T-28 pass are shown at the top of Fig. 5. Irregularly shaped graupel particles with maximum diameters of $\sim$0.5 cm were detected in the largest concentrations near the edges of updraft U2 as well as in the adjacent downdrafts (D1 and D2). The hail spectrometer, sampling a larger volume ($\sim$200 $m^3$ over 2 km of flight), recorded particles with diameters of up to 1 cm in this same region. Throughout this entire

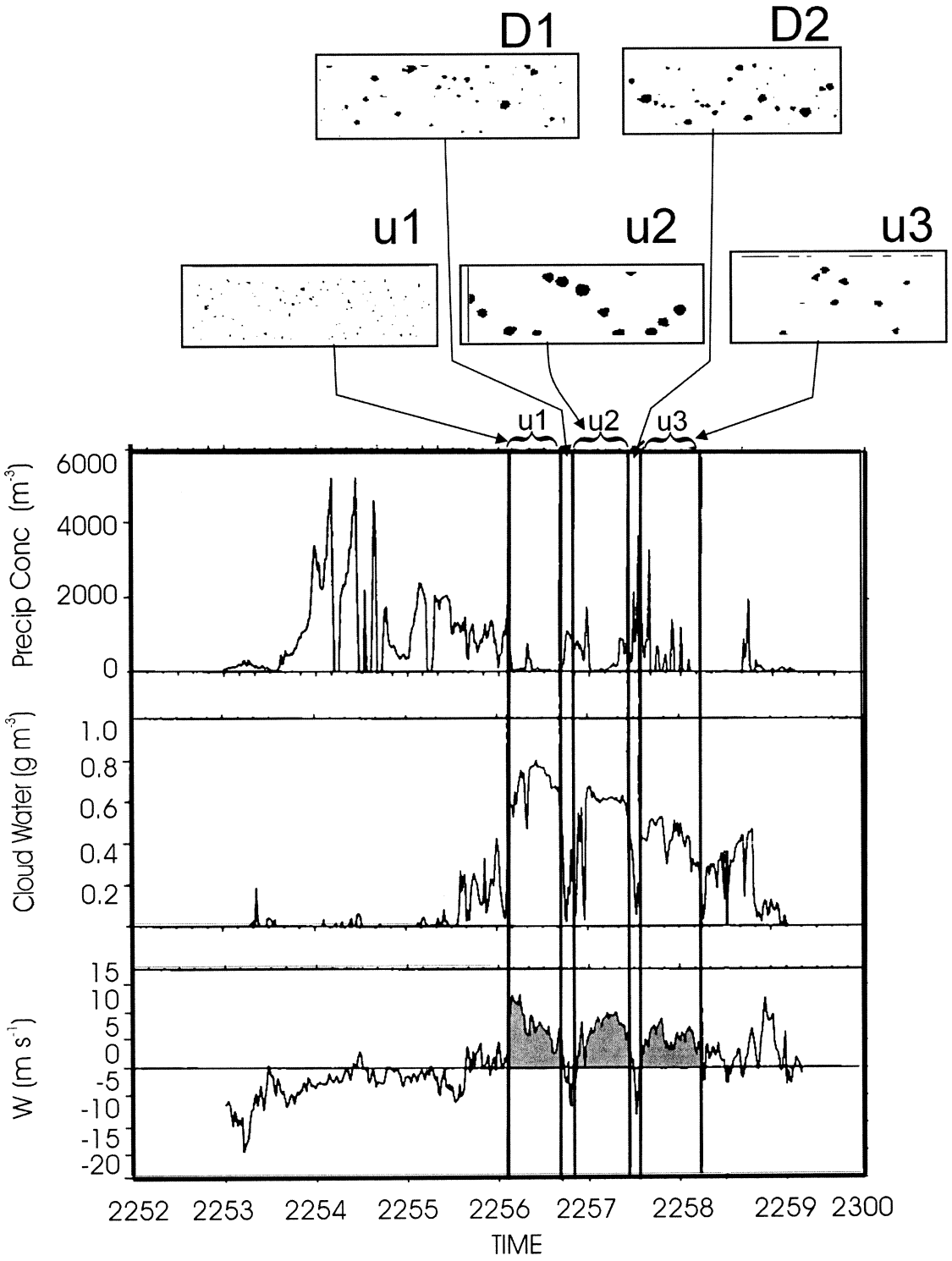


FIG. 5. Selected T-28 in situ data. (top) 2D particle images are from the HVPS probe; u1, D1, etc., identify updraft and downdraft areas, respectively. The vertical height of the image frames represents 4.5 cm. From top to bottom, the stacked panels depict the time variation of 1) precipitation-sized (diameter $> 200$ $\mu$m) particle concentration ($m^{-3}$) from the HVPS optical probe, 2) cloud liquid water concentration ($g\ m^{-3}$) from the King liquid water probe, and 3) vertical air velocity ($m\ s^{-1}$) derived from aircraft altitude and performance data.

period, the microphone attached to the T-28's forward windscreen did not record any of the sharp ''bangs'' or distinct ''pings'' that are associated with high-density ice-particle impacts (Jameson and Heymsfield 1980). It is improbable that droplets grown from initial nucleation during an ascent directly from cloud base could have resulted in such large, low-density ice hydrometeors during the approximately 10-min transit time required to reach the T-28's altitude (Rockicki and Young 1978). It is more likely that these large ice particles originated at higher altitudes and were carried to the T-28's vicinity by the downdrafts (i.e., D1 and D2) that were imbedded in the general storm-inflow region. They may also have fallen out of the overhanging anvil region on the south side of the storm and reentered the updraft at lower levels. The modest densities of these particles resulted in relatively low terminal velocities, permitting them to be carried readily upward by the stronger updrafts.

Overall, the in situ observations at the T-28's altitude show that the storm inflow region contained adjacent small-scale up- and downdrafts with characteristic diameters of 1–3 km (i.e., too small to be faithfully resolved in the dual-Doppler flow fields). The downdrafts contained the highest concentrations of fairly low-density ice particles with maximum dimensions approaching 1 cm. Some of these large particles appeared to be mixing into the adjacent updrafts. The presence of such large ice particles in the storm-inflow region suggests that they may have served as embryos upon which hailstones subsequently grew as they rose into the updraft.

## 4. Trajectory calculations

To explore possible associations between the up-to-centimeter-sized ice particles observed by the T-28 at 2257 and the HDR hail signature that appeared around 2303, particle-trajectory calculations based on the dual-Doppler wind fields were done. The details of this trajectory model are given in Knight and Knupp (1986). In general, the model uses microphysically simple representations of ice-particle growth processes [as compared with the more complete treatment in, e.g., Heymsfield (1983)]. All particles are taken to be spherical with a collection efficiency of 1. The particle terminal fall speeds are calculated using a fixed drag coefficient. The particle bulk density is taken to be a function of radius according to

$$\rho(R) = 0.211R + 0.489, \quad (3)$$

where $\rho$ is the ice particle density (g cm$^{-3}$) and $R$ (cm) is the radius. The density increase with radius in Eq. (3) represents the growth of graupel particles from aggregates. The particles grow by simple geometric sweep out. In-cloud liquid water content (LWC) deviations from the adiabatic limit are based on the local updraft magnitude and air temperature. In particular, adiabatic LWC is assumed to exist when updraft speed exceeds 10 m s$^{-1}$; LWC is linearly reduced to 0 as updraft speeds decrease from 10 to 0 m s$^{-1}$. In addition, to represent the effects of glaciation, the updraft-modulated LWC is linearly reduced to 0 as the temperature decreases from $-20°$ to $-40°$C. The trajectory calculations assume that the particles are at their terminal fall velocity as they advect with the three-dimensional dual-Doppler wind field. Growth takes place according to the parameterized LWC mass intercepted per calculation time step. At the end of each time step, an updated terminal velocity is computed using the augmented mass. Note that this trajectory model does not include melting. Frozen particles that move below the melting level merely maintain their size, rather than ultimately collapsing into a liquid drop. These assumptions are admittedly simple, but the results of Knight and Knupp (1986) have demonstrated that this trajectory model can provide useful insights into the source and fallout regions of frozen hydrometeors.

In this analysis, both forward and backward trajectories were started from a 2 km $\times$ 2 km box centered on the 2257 T-28 location. The basic three-dimensional storm-relative wind fields were obtained from dual-Doppler analyses valid at 2241, 2247, 2252, and 2306. The observed echo motion was used to advect horizontally the individual dual-Doppler analyses to a common reference time of 2257. The gaps in the synthesized wind field input sequence were filled by a simple time-weighted interpolation procedure. This procedure allowed the wind fields being used in the trajectory program to be updated at approximately 5-min intervals during the calculations. The trajectories were computed using a time step of 10 s.

A number of trajectory model runs were made to test the sensitivity of the results to uncertainties in the various input parameters. The input parameters that were varied in the sensitivity tests included 1) a multiplicative adjustment to the LWC values, 2) the coefficients relating density to radius, and 3) the ice-particle drag coefficient. The sensitivity tests were primarily conducted by examining the endpoints of the forward trajectories in relationship to the observed 1.8-km HDR hail signature location (as advected to the 2257 reference time).

Only some general results of the sensitivity tests will be presented. Following Knight and Knupp (1986), a test of the cloud liquid water parameterization was performed by uniformly increasing the LWC values by 50%. This change generally only altered the trajectory endpoint locations by 1–2 km. This insensitivity was primarily due to modest updraft magnitudes and durations that the trajectory paths encountered. (Recall that the LWC is parameterized as a function of updraft strength and temperature.) Because of this limited variation, the original Knight and Knupp (1986) LWC formulation was retained.

To represent lower ice-particle bulk densities, particularly at smaller diameters, an alternative density-versus-size relationship was tested:

$$\rho(R) = 0.8R + 0.1. \quad (4)$$

The symbols have the same meanings as in Eq. (3). The use of Eq. (4) had a negligible effect on the hail fallout locations at the endpoints of the forward trajectories. The origination points of the backward trajectories shifted by 1–2 km, but they remained within the same general portion of the multicell system. (The midlevel echo region is located above the inflow area.) Equation (3) [as was also used by Knight and Knupp (1986)] was ultimately selected as the ice-density specification.

The drag coefficient was varied between 0.3 and 1.5, a range generally representative of ice particles under large-Reynolds-number conditions (Foote 1984). Larger drag coefficients reduce the particle terminal velocities and result in trajectories that more nearly follow the air motion field. A drag coefficient of 0.9 was selected for use in these trajectory calculations. This value is consistent with that measured by Knight and Heymsfield (1983) for ~1-cm-diameter hailstones with an average bulk density of 0.44 g $cm^{-3}$.

The detailed results of the trajectory calculations are influenced by a large number of incompletely known factors. Nevertheless, a broadly repeatable pattern of trajectories emerged during the sensitivity tests. The forward trajectories consistently lead from the 2257 T-28 location to the general vicinity (typically within 2–4 km) of the 2304–2308 HDR hail signature at 1.8 km MSL. The trajectory endpoint times were also in general agreement with the times at which the HDR hail signature was observed. (See the tabular summary at the bottom of Fig. 6.) Many of the backward-trajectory results were invalid because of their descent below the melting level (4.56 km MSL). (This was most true of particles that were initialized in the stronger updrafts. During the backward-trajectory calculations, these particles descended the most rapidly to the melting level. Because the model does not consider melting, trajectories that reached the 0°C level were disregarded.) The backward trajectories that remained at subfreezing temperatures originated in the ~7.5-km-MSL height region in the forward part of the echo system.

A plan view of a representative set of trajectories is included as the dark solid lines in Fig. 6. Particles of 0.8-cm diameter were launched from the 2 km × 2 km box centered at $X = 33$, $Y = -38$ km. The forward trajectories curve toward the southwest and terminate in the general vicinity of the plus symbols that mark the >0-dB HDR grid points. The table in the lower portion of the figure summarizes the trajectory endpoint information. Most of the trajectory endpoints are in fair agreement with the CSU–CHILL HDR hail signature observations. As noted earlier, this hail signature was located over very thinly populated countryside, and so no verification observations are available.

As a secondary check on these trajectory results, an additional set of backward trajectories was calculated from an initiation area within the HDR signature region, shown by the plus symbols in Fig. 6. To get a categorical indication of the hail diameters, vertical profiles of $Z_{dr}$ at heights below the 0°C level were examined within the positive HDR hail signature. The horizontally averaged $Z_{dr}$ within the HDR signature became more positive with decreasing height. This was most true in the 2208 volume, when the $Z_{dr}$ at the 1.8-km height level reached 1.3 dB. Aydin et al. (1990) have shown that such an increasing $Z_{dr}$ trend in the descending precipitation shaft may indicate the presence of hailstones that are undergoing significant (and in some cases complete) melting. Under the broad assumption that this indication of significant melting implied relatively small hail diameters, the backward trajectories were initiated with a particle diameter of 1 cm. In agreement with the forward-trajectory results, these backward trajectories generally linked the HDR hail signature with the storm region sampled by the T-28 at 2257. (At the backward time step corresponding to 2257, the distance between the mean particle trajectory locations and the T-28 was 2 km horizontally and 0.8 km vertically.)

The primary backward trajectories were initiated from the T-28's location at 2257. Three of these trajectories remained at subfreezing temperatures and generally terminated in an area 5–8 km southeast of the 2257 T-28 position at altitudes between 7 and 8.5 km MSL. Thus, this midlevel portion of the storm may have been a source region for some of the particles that were detected by the aircraft and subsequently fell out as hail near the HDR hail signature. The overall shape of the early trajectories suggests that when the particles were at these higher altitudes, they had a small northeastward motion component. Their movement shifted toward the northwest as they descended into the general storm-inflow region.

A vertical cross section aligned with the particle trajectories is shown in Figs. 7a and 7b. The basic storm reflectivity structure and dual-Doppler-based wind field are shown in Fig. 7a. To characterize the overall situation around the 2257 reference time, the radar data fields shown in Fig. 7a are averages of the gridpoint values in the individual 2306 and 2252 analyses. Based on the cross section, the T-28 was flying through reflectivities somewhat above 30 dB*Z* in the forward overhang region of the storm. The synthesized updraft magnitudes agree well with the peak updrafts of approximately 10 m $s^{-1}$ that the T-28 recorded in updraft U2 (see Fig. 5). The projections of the particle trajectories onto this vertical cross section are shown in Fig. 7b. The overall trajectory pattern suggests that the modeled particles were reversing their vertical motion in the vicinity of the T-28 as the descent from their origins at higher altitudes ended and they became entrained into the primary updraft circulation.

## 5. Discussion

During the analyzed time period, the reflectivity patterns indicated that the 22 June 1998-storm was a multicell system of the ''strong evolution'' category, as out-

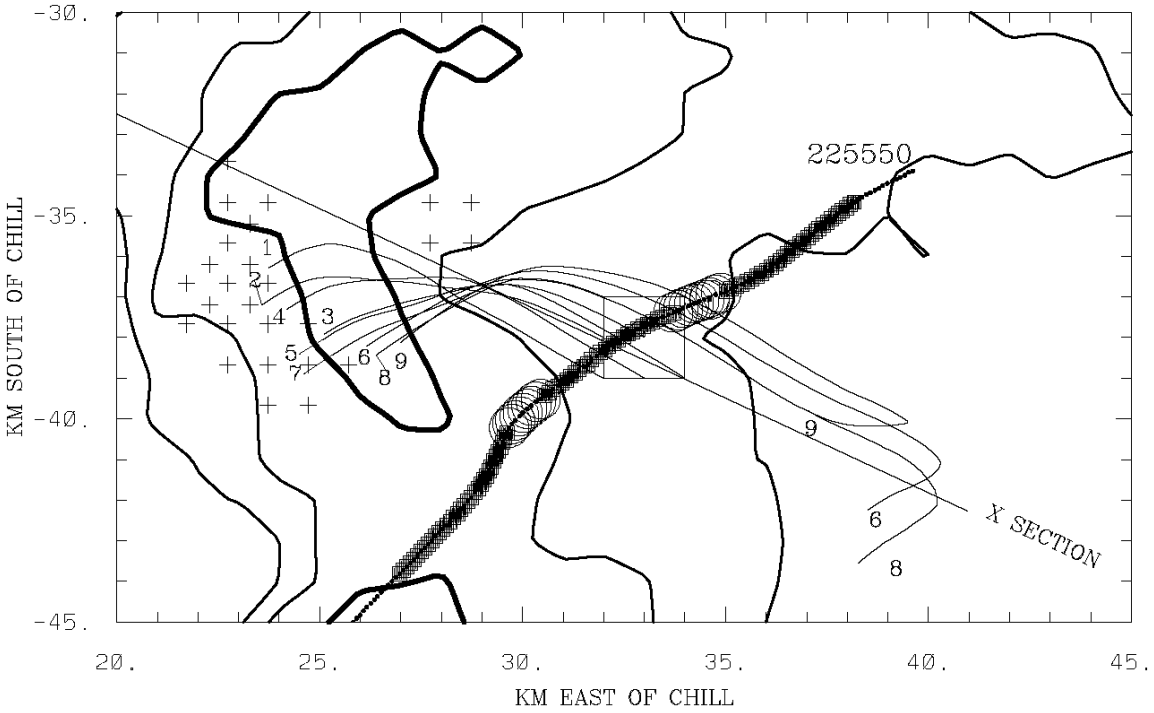


| TRAJ NUM | FORWARDS | | | BACKWARDS | | |
|---|---|---|---|---|---|---|
| | HGT(KM) | TIME(UTC) | DIA(CM) | HGT(KM) | TIME(UTC) | DIA(CM) |
| 1 | 2.0 | 230819 | 1.12 | | | |
| 2 | 1.8 | 230719 | 0.86 | | | |
| 3 | 2.2 | 230449 | 0.81 | | | |
| 4 | 2.0 | 230819 | 1.09 | | | |
| 5 | 2.0 | 230619 | 0.87 | | | |
| 6 | 2.1 | 230449 | 0.83 | 7.5 | 223911 | 0.20 |
| 7 | 1.9 | 230749 | 0.99 | | | |
| 8 | 2.0 | 230549 | 0.88 | 7.1 | 223911 | 0.13 |
| 9 | 1.8 | 230449 | 0.83 | 8.4 | 223911 | 0.21 |

FIG. 6. Plan view of computed particle trajectories plotted on the 4.8-km-height-level CSU–CHILL reflectivity pattern at 2257 UTC. (Reflectivity contour plotting conventions are as in Fig. 2.) Forward and backward trajectories (curved dark solid lines) are initiated with 0.8-cm-diameter ice particles released from the square region centered at $X = 33$, $Y = -38$, and $Z = 4.8$ km. Trajectories are numbered at their endpoints. The table in the lower portion of the figure summarizes the data at the trajectory endpoints. (Note: backward trajectories that descend to heights below the 0°C level are not considered.) Cross symbols mark the 1.8-km-MSL grid points at which HDR values exceeded 0 dB at 2204 (gray crosses) and 2208 UTC (black crosses). These gridpoint locations have been horizontally advected to the common storm-relative trajectory reference time (2257). (Note: the HDR data are from the 1.8-km height level; the reflectivity contours are from the T-28 4.8-km height level. As a result, the HDR-depicted hail area appears outside of the 50-dB*Z* reflectivity contour.) The angled solid gray line marks the location of the vertical cross section shown in Figs. 7a,b.

lined by Foote and Frank (1983). To be specific, the dual-Doppler and reflectivity analyses implied that neither the echo core nor the main updraft associated with the newer cell in the southern end of the echo complex ever appreciably merged with the neighboring older core that was central to this study. (These two cells were joined at reflectivity levels of ~30 dBZ.) The trajectory calculations suggest that low-density graupel particles in the midlevel region of the echo complex descended into the underlying storm inflow and were subsequently ingested into the northern cell. The final growth of these particles into small hail took place in the northern cell's updraft. More detailed analyses of the hail growth processes are not possible in this case because of the coarse time and space resolution in the available dual-Doppler wind fields. Nevertheless, the basic hail growth process identified here, the transport of externally grown embryos into an updraft in which their final growth takes place, has been identified in earlier studies (Heymsfield et al. 1980; Ziegler et al. 1983; Heymsfield 1983). The case presented here, however, is the first involving direct observations of recirculating embryos reentering the base of a mature updraft.

The microphysical characteristics of the three discrete updraft regions encountered by penetrating aircraft were different from each other. Updraft U1 showed little sign of ingestion of previously grown embryos but showed evidence of an active coalescence process leading to

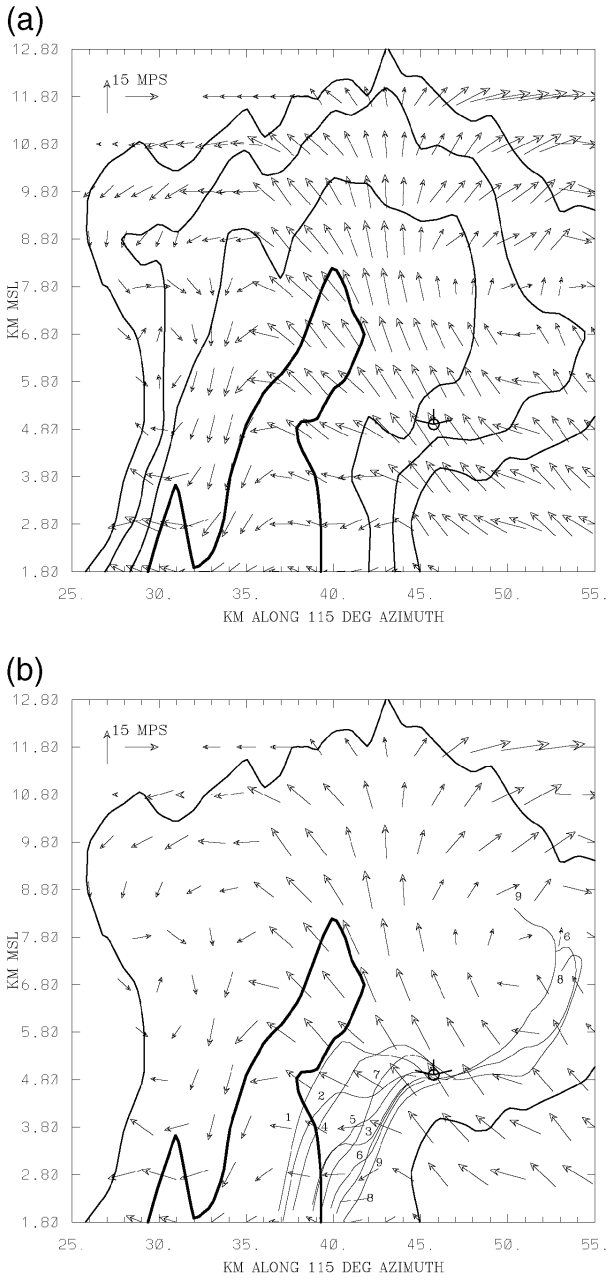


FIG. 7. (a) Vertical cross section generally aligned with the particle trajectories. The reflectivity contours and storm-relative dual-Doppler wind vectors are an average of the gridpoint values in the 2306 and 2252 analyses. Reflectivity contours start at 20 dBZ and increase in 10-dB steps; the 50-dBZ contour is thickened. Velocity vector scales are in the upper left. The projection of the T-28's 2257 location onto the cross-sectional plane is shown schematically. (b) Vertical cross section that includes the particle trajectories. The reflectivity contours and airflow vectors are simplified versions of those shown in (a). Particle trajectories are plotted as solid lines. Trajectories are identified by number.

drizzle. Updraft U2 contained large irregular-looking particles that were probably graupel or rimed aggregates ingested after descending from the upshear overhang from the neighboring cell to the south or from the narrow downdrafts that flank this updraft region. Updraft U3, closest to the neighboring southern cell, contained smaller rough-looking particles, again probably ingested from the overhang region or from the flanking narrow downdraft regions.

## 6. Conclusions

The T-28 research aircraft encountered regions of ~1-cm-diameter low-density graupel particles as it traversed the inflow area of a multicell thunderstorm system. Particle forward-trajectory calculations initiated from the T-28's observations indicate that these graupel particles subsequently grew as they passed through a weakening updraft and landed within a few kilometers of a polarimetric radar hail signature. Backward trajectories that were also initiated from the T-28's location imply that some of the hail embryos originated in the midlevel regions downstream of a neighboring cell. From this initiation region, the particles descended into the inflow of the cell in which their final growth into small hailstones took place. Although not resolved by the trajectory model, large particles that reached the T-28's position from heights below the 0°C level could also serve as hail embryos. In a similar way, the several narrow, particle-laden downdrafts observed by the T-28 within the general storm-inflow area were too small to be resolved in the dual-Doppler wind field synthesis. Thus, the source region of the larger ice particles that these downdrafts were carrying could not be determined.

The combined aircraft–radar dataset that was obtained on 22 June 1998 demonstrates the complexity of hail production in time-evolving multicell thunderstorms. Although the T-28 encountered several bursts of centimeter-diameter graupel within the general storm-inflow region, only those particles that were positioned so that they could be drawn into an established updraft were able to complete their growth into hail. However, this updraft was weakening with time, and so effective hail production was further restricted to those embryos that reached the older updraft while its areal extent and intensity were still capable of providing adequate final hail-growth conditions (Nelson 1983).

Continuing aircraft and polarimetric radar observations of hailstorms in various organizational categories will reveal further details of the multiple processes through which thunderstorms generate hail and the relative frequency with which various general growth trajectories occur.

*Acknowledgments.* The journal reviewers, including L. J. Miller (NCAR), suggested a number of useful improvements to this paper. We also appreciate the reviews of the first draft of this paper that were provided by S.

Rutledge (CSU), P. Smith (SDSMT), and C. Knight (NCAR). The trajectory program was made operable through the efforts of John Tuttle (NCAR). Among the SDSMT staff, aircraft data-analysis software support was provided by Rand Feind and Donna Kliche; Fig. 5 was prepared by Connie Crandall. This research was funded through the National Science Foundation Grant ATM-9500108 (CSU–CHILL Radar Facility), and Grants ATM-9618569 and ATM-0099344 (armored T-28 aircraft facility for research requiring storm penetration).

## REFERENCES

Aydin, K., T. A. Seliga, and V. Balaji, 1986: Remote sensing of hail with dual linear polarization radar. *J. Climate Appl. Meteor.*, **25,** 1475–1484.

——, Y. Zhao, and T. A. Seliga, 1990: A differential reflectivity hail measurement technique: Observations during the Denver hailstorm of 13 June 1984. *J. Atmos. Oceanic Technol.*, **7,** 104–113.

Barnes, S. L., 1980: Report on a meeting to establish a common Doppler radar data exchange format. *Bull. Amer. Meteor. Soc.*, **61,** 1401–1404.

Brunkow, D., V. N. Bringi, P. C. Kennedy, S. A. Rutledge, V. Chandrasekar, E. A. Mueller, and R. K. Bowie, 2000: A description of the CSU–CHILL national radar facility. *J. Atmos. Oceanic. Technol.*, **17,** 1596–1608.

Cressman, G. P., 1959: An operational objective analysis scheme. *Mon. Wea. Rev.*, **87,** 367–374.

Crum, T. D., R. L. Alberty, and D. W. Burgess, 1993: Recording, archiving, and using WSR-88D data. *Bull. Amer. Meteor. Soc.*, **74,** 645–653.

Dye, J. E., B. E. Martner, and L. J. Miller, 1983: Dynamical-microphysical evolution of a convective storm in a weakly sheared environment. Part I: Microphysical observations and interpretation. *J. Atmos. Sci.*, **40,** 2083–2096.

Foote, G. B., 1984: A study of hail growth utilizing observed storm conditions. *J. Climate Appl. Meteor.*, **23,** 84–101.

——, and H. W. Frank, 1983: Case study of a hailstorm in Colorado. Part III: Airflow from triple-Doppler measurements. *J. Atmos. Sci.*, **40,** 686–707.

Heymsfield, A. J., 1983: Case study of a hailstorm in Colorado. Part IV: Graupel and hail growth mechanisms deduced through particle trajectory calculations. *J. Atmos. Sci.*, **40,** 1482–1509.

——, A. R. Jameson, and H. W. Frank, 1980: Hail growth mechanisms in a Colorado storm. Part II: Hail formation processes. *J. Atmos. Sci.*, **37,** 1779–1807.

Jameson, A. R., and A. J. Heymsfield, 1980: Hail growth mechanisms in a Colorado storm. Part I: Dual-wavelength radar observations. *J. Atmos. Sci.*, **37,** 1763–1778.

Jayaweera, K. O. L. F., and B. J. Mason, 1965: The behavior of freely-falling cylinders and cones in a viscous fluid. *J. Fluid Mech.*, **22,** 709–725.

Johnson, G. N., and P. L. Smith Jr., 1980: Meteorological instrumentation system on the T-28 thunderstorm research aircraft. *Bull. Amer. Meteor. Soc.*, **61,** 972–979.

Knight, C. A., and K. R. Knupp, 1986: Precipitation growth trajectories in a CCOPE storm. *J. Atmos. Sci.*, **43,** 1057–1073.

Knight, N. C., and A. J. Heymsfield, 1983: Measurement and interpretation of hailstone density and terminal velocity. *J. Atmos. Sci.*, **40,** 1510–1516.

Miller, L. J., J. E. Dye, and B. E. Martner, 1983: Dynamical-microphysical evolution of a convective storm in a weakly sheared environment. Part II: Airflow and precipitation trajectories from Doppler radar observations. *J. Atmos. Sci.*, **40,** 2097–2109.

——, J. D. Tuttle, and C. A. Knight, 1988: Airflow and hail growth in a severe northern High Plains supercell. *J. Atmos. Sci.*, **45,** 736–762.

——, ——, and G. B. Foote, 1990: Precipitation production in a large Montana hailstorm: Airflow and particle growth trajectories. *J. Atmos. Sci.*, **47,** 1619–1646.

Mohr, C. G., L. J. Miller, R. L. Vaughan, and H. W. Frank, 1986: On the merger of mesoscale data sets into a common Cartesian format for efficient and systematic analysis. *J. Atmos. Oceanic Technol.*, **3,** 143–161.

Nelson, S. P., 1983: The influence of storm flow structure on hail growth. *J. Atmos. Sci.*, **40,** 1965–1982.

Pruppacher, H. R., and K. V. Beard, 1970: A wind tunnel investigation of the internal circulation and shape of water drops falling at terminal velocity in air. *Quart. J. Roy. Meteor. Soc.*, **96,** 247–256.

Rockicki, M. L., and K. C. Young, 1978: The initiation of precipitation in updrafts. *J. Appl. Meteor.*, **17,** 745–754.

Wood, V. T., and R. A. Brown, 1997: Effects of radar sampling on single-Doppler velocity signatures of mesocyclones and tornadoes. *Wea. Forecasting*, **12,** 928–938.

Ziegler, C. L., P. S. Ray, and N. C. Knight, 1983: Hail growth in an Oklahoma multicell storm. *J. Atmos. Sci.*, **40,** 1768–1791.